Elastic and hydrodynamic torques on a colloidal disk within a nematic liquid crystal

Joel B. Rovner, Dan S. Borgnia, Daniel H. Reich, and Robert L. Leheny

Department of Physics and Astronomy, Johns Hopkins University, Baltimore, Maryland 21218, USA

The orientationally dependent elastic energy and hydrodynamic behavior of colloidal disks with homeotropic surface anchoring suspended in the nematic liquid crystal 4-cyano-4′-pentylbiphenyl (5CB) have been investigated. In the absence of external torques, the disks align with the normal of the disk face $\hat{a}$ parallel to the nematic director $\hat{n}$. When a magnetic field is applied, the disks rotate $\hat{a}$ by an angle θ so that the magnetic torque and the elastic torque caused by distortion of the nematic director field are balanced. Over a broad range of angles, the elastic torque increases linearly with θ in quantitative agreement with a theoretical prediction based on an electrostatic analogy. When the disks are rotated to angles $\theta > \frac{\pi}{2}$, the resulting large elastic distortion makes the disk orientation unstable, and the director undergoes a topological transition in which $\theta \longrightarrow \pi - \theta$. In the transition, a defect loop is shed from the disk surface, and the disks spin so that $\hat{a}$ sweeps through π radians as the loop collapses back onto the disk. Additional measurements of the angular relaxation of disks to $\theta = 0$ following removal of the external torque show a quasi-exponential time dependence from which an effective drag viscosity for the nematic can be extracted. The scaling of the angular time dependence with disk radius and observations of disks rotating about $\hat{a}$ indicate that the disk motion affects the director field at surprisingly modest Ericksen numbers.

PACS number(s): 61.30.Jf, 61.30.Gd, 82.70.Dd

I. INTRODUCTION

In liquid crystals the introduction of interactions and constraints that compete with the fluid's Frank elastic energy result in a number of emergent phenomena. Examples include the Fréederieksz transition, where electric or magnetic field energies conflict with the elasticity [1], and the formation of blue phases in chiral nematics, which results from the incompatibility of global space filling with the strain-minimizing double-twist structure [1,2]. When inclusions are added to a nematic, interactions at the inclusion surfaces impose boundary conditions on the liquid-crystal order that similarly constrain the ordering, leading to distorted director fields and the formation of topological defects [3], as exemplified by the canonical 'Saturn rings" and "hedgehog" defects that accompany a spherical colloid with homeotropic anchoring in a nematic [4,5]. Further, since changes in the relative position of multiple inclusions can change the energy cost associated with these distortions, an effective force between inclusions is created [6]. At large distances, the form of this interaction is dictated by the symmetry of the nematic distortions, leading typically to anisotropic attractive forces between suspended particles. This property of liquid crystals has been advanced as a method for colloidal self-assembly and the fabrication of metamaterials [6].

While the vast majority of research on inclusions in liquid crystals has concerned spherical particles, several studies have revealed new phenomena that emerge with nonspherical particles [7–22]. For example, Lapointe and coworkers have found that equilateral polygonal platelets assemble in a nematic via either dipolar or quadrupolar forces depending on the number of polygon sides and that the elastic forces on cylindrical inclusions can be used to position the particles with high precision [7,12]. An important parameter for aspherical particles in liquid crystals is the particle orientation with respect to the liquid-crystal order since changes in the orientation can alter the elastic energy, leading to new forms of forces and interactions [13]. As with the pair interaction between two

particles produced by the distortions, an aspherical particle will experience a torque that seeks to rotate it to the orientation with the lowest distortion energy. This behavior has been explored previously in rod-shaped inclusions and less thoroughly in platelets, leading to a number of insights into the physical effects liquid crystals can have on inclusions [12,14–16,23]. To understand more fully the orientation-dependent properties of aspherical particles in liquid crystals, we have investigated experimentally the behavior of isolated disk-shaped inclusions with homeotropic anchoring in a nematic. One motivation for this work is to explore how the director-field distortion around a suspended particle can be controlled through its orientation, thereby tuning elastically mediated colloidal interactions [12]. We find that for modest deviations in disk orientation from the minimum energy, the disks impose an elastic energy cost on the nematic that quantitatively follows a form similar to that obtained previously for rod-shaped colloids with longitudinal anchoring [14] and that can be understood in terms of an electrostatic analogy [24]. However, unlike with the rod-shaped colloids, the disks do not support a metastable director distortion at larger deviations. For large deviations an instability drives a topological transition in the director field to a lower-energy state. Additional measurements examining the dynamic response of disks and the surrounding director field to changes in external torque reveal viscous properties of the nematic that suggest the disk motion affects the director field at surprisingly modest angular velocities.

II. EXPERIMENTAL PROCEDURES

A. Disk fabrication

Ferromagnetic Ni disks with radii $R = 5$ and 20 μm and thickness $L = 300$ nm were fabricated using contact photolithography. First, a thin sacrificial layer of poly(methyl methacrylate) (PMMA) was applied via spin coating to a glass slide, and the slide was heated to cure the PMMA. A 300 nm thick film of nickel was sputtered on top of the

PMMA, and a layer of a positive photoresist was applied via spin coating atop the nickel. Disks were patterned from the Ni film via standard photolithography and etching of the Ni with a nitric acid solution. Detachment of the disks from the substrate was achieved by dissolving the PMMA layer and the remaining photoresist in acetone. A rare earth magnet was subsequently used to separate the disks from the acetone solution. The disks were then repeatedly sonicated and rinsed in acetone and isopropanol to clean them thoroughly. In the presence of sufficiently low magnetic fields, $B < 10$ G, the 5 μm disks possess a magnetic moment $\vec{\mu}$ in the plane of the disk of magnitude $(1.6 \pm 0.3) \times 10^{-12}$ A m^2 as determined by their translational response [25] to magnetic-field gradients in silicone oil of known viscosity. The quoted uncertainty in $\vec{\mu}$ reflects the disk-to-disk variation from measurements on multiple disks. Measurements of $\vec{\mu}$ for the 20 μm disks revealed a nonlinear, field-dependent moment even at applied fields below 10 G. Therefore, all experiments requiring quantitative knowledge of $\vec{\mu}$ were restricted to the 5 μm disks.

A silane layer of N-octadecyldimethyl[3-(trimethoxysilyl)propyl]ammonium chloride (DMOAP; UCT Specialties) was used to produce homeotropic anchoring on the surfaces of the disks following a procedure described by Noel *et al.* [26]. The disks were sonicated in a 2% solution of DMOAP in deionized water. Subsequent washing of the disks in isopropanol removed any excess DMOAP. After washing, the alcohol was removed, and the disks were heated at 110 °C for 1 h and then were resuspended in isopropanol. The disks were suspended in the liquid crystal 4-cyano-4′-pentylbiphenyl (5CB; Kingston Chemicals; purity >99.8%) by using a rare earth magnet to hold the disks in place within the vial while decanting and evaporating residual isopropanol before replacing it with 5CB. The liquid crystal and disk solution was then sonicated and introduced through capillary action into liquid-crystal cells composed of parallel glass slides separated by 80 μm and treated either with DMOAP for homeotropic anchoring or with rubbed polyimide for uniform planar anchoring.

B. Optical microscopy with *in situ* magnetic field

The behavior of the disks in nematic 5CB was investigated with polarized light microscopy using an inverted microscope (Nikon TE2000-E) with an extra-long working distance (40×/0.60) objective. A two-axis set of Helmholtz coils was mounted on the microscope to produce magnetic fields of uniform magnitude in the field of view. One set of coils produced fields parallel to the microscope optical axis (i.e., vertical), and the other produced fields parallel to the microscope focal plane (i.e., horizontal). The axis of the horizontal coils was aligned with the horizontal component of earth's magnetic field to enable canceling of earth's field. The coils produced fields from 0 to 10 G at arbitrary angles to the vertical with a precision of ±0.05 G. The static orientation of disks in the 5CB and their dynamic response to applied magnetic fields was monitored with video microscopy using either a standard video camera (Nikon, D3100) or high-speed camera (Photron, FASTCAM 512PCI). Transmission microscopy images of the disks revealed elliptical shapes whose eccentricity depended on the orientation of the normal

to the disk face $\hat{a}$ with respect to the microscope focal plane (see inset to Fig. 2). Analysis of such images to obtain disk orientation was performed in the software package IGOR Pro. For orientations in which the disk was tilted significantly out of the focal plane, the images were distorted. These distortions were kept to a minimum by using a microscope objective with a large depth of field but nevertheless required correction in some cases. To correct for such distortions, images of a disk in an isotropic fluid with applied magnetic fields of known orientation were obtained. In the isotropic fluid, the disk's magnetic moment aligns with the applied field so that the disk orientation is known. From a set of such images at various disk orientations, a mapping between measured ellipse eccentricity and angle of tilt of the disk out of the focal plane was obtained. This mapping was then used to determine disk orientations in analysis of images of the disks in nematic 5CB. All measurements were performed at room temperature in the nematic phase of 5CB.

III. RESULTS AND DISCUSSION

A. Elastic torque

In the absence of any external torques, disks with homeotropic anchoring align with the normal to the disk faces, specified by the vector $\hat{a}$, parallel to the far field director $\hat{n}$. Neglecting the disk edges, in this orientation the homeotropic anchoring at the disk surfaces is satisfied without any distortion of the surrounding director field, as shown schematically in Fig. 1(a), and indeed polarization microscopy on such disks reveals no birefringent texture that would indicate director distortions. When a uniform magnetic field $\vec{B}$ is applied, the disk experiences a torque, $\vec{\tau}_B = \vec{\mu} \times \vec{B}$, that causes $\vec{\mu}$ and hence $\hat{a}$ to rotate, leading to distortion of the director, as depicted schematically in Fig. 1(b). The elastic energy U associated with this distortion depends on the angle of rotation θ, and therefore the disk feels a restoring elastic
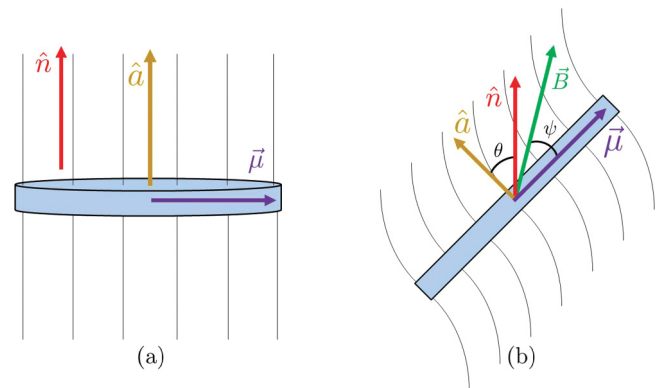

FIG. 1. (Color online) Schematics of a ferromagnetic Ni disk with homeotropic surface anchoring in a nematic liquid crystal. The thin black lines depict the director field in the vicinity of the disk. The disk's permanent magnetic moment $\vec{\mu}$ is parallel to the disk face. (a) In the absence of external torques, the disk orients such that the unit vector $\hat{a}$ perpendicular to its face is parallel to the far-field director $\hat{n}$. (b) When a magnetic field $\vec{B}$ is applied, the disk rotates $\hat{a}$ to an angle θ with respect to the far-field director at which the magnetic and elastic torques are balanced.
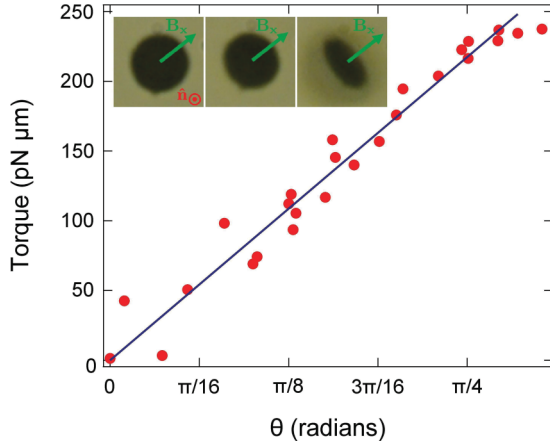
FIG. 2. (Color online) Elastic torque on a 5 μm Ni disk with homeotropic anchoring in 5CB as a function of the angle between the normal to the disk face and the far-field director. The torque follows a linear dependence implying a quadratic growth in elastic energy with angle, $U \propto \theta^2$. The three insets illustrate the projected elliptical shape of a 5 μm disk viewed through the microscope for angles of $\theta \approx \pi/16$, $\pi/9$, and $\pi/3$. These three disk angles were produced by varying B_z, the component of the magnetic field parallel to the director while keeping constant B_x, the component of the field in the focal plane whose unit vector is denoted by the green arrow.

torque, $|\vec{\tau}_E| = \frac{\partial U}{\partial \theta}$. Following application of an applied field, the disk comes to rest when the magnetic and elastic torques are balanced:

$$|\vec{\tau}_E(\theta)| = |\vec{\tau}_B| = |\vec{\mu}||\vec{B}| \sin \psi, \qquad (1)$$

where ψ is the angle between $\vec{B}$ and $\vec{\mu}$ as shown in Fig. 1(b). By varying the magnitude and direction of the magnetic field, we have mapped out the elastic torque on a disk as a function of θ. Figure 2 displays results for the torque on a 5 μm disk as a function of θ. Over a broad range of angles, the torque grows linearly with θ, $|\vec{\tau}_E| = A\theta$, implying $U = \frac{1}{2}A\theta^2$. The solid line in Fig. 2 is the result of a linear fit over the range $0 < \theta \lesssim \frac{\pi}{4}$. From these results and similar measurements on other 5 μm disks, the proportionality constant was determined to be $A = (220 \pm 70)$ pN μm/radian, where the uncertainty is dominated by the variability in the magnetic moment of the disks. Measurements of the torque at $\theta > \pi/4$ were consistent with the linear trend in Fig. 2 extending to larger angle. However, because of the instability described in Sec. III B, these measurements required field orientations with smaller ψ, leading to greater uncertainty in the resulting torque. Hence, we restrict our quantitative analysis of the torque to $\theta \leqslant \pi/4$. The measurements include disks in both homeotropic and planar cells, for which the disk orientation at $\theta = 0$ with respect to the microscope focal plane is different. Good agreement in the torque values is seen in the two cases, indicating that the image correction procedure mentioned in Sec. II B is accurate.

We note that the influence of the bounding substrates could be observed in the experiments following prolonged periods during which $\theta = 0$. Due to the large density of Ni, disks at $\theta = 0$ would sediment to the bottom substrate. However, when rotated away from $\theta = 0$, they would rise by several micrometers in the cells. This effect was more clearly visible in

homeotropic cells. Due to the boundary condition at the bottom substrate, a disk that rotates away from $\theta = 0$ will introduce a distortion in the director concentrated between the underside of the disk and the substrate. The energy cost of this distortion is reduced if the distance between the disk and substrate is increased, leading to a repulsive force. As a result, the disk levitates to a height at which this repulsive force is balanced by gravity. Such levitating interactions between colloids and substrates have been investigated previously [14,15,27], and we did not explore it in detail in this case. Nevertheless, a consequence of the interaction was to free disks from the vicinity of the substrate so that they rotated freely about an axis through their center when θ was varied. As a result, as the good agreement in the torque values measured in homeotropic and planar cells confirms, the measured torque was not substantially affected by the proximity of the substrates.

A previous experiment by Hayes measuring the torque on coagulated magnetic grains that form soft platelets in a nematic observed a linear dependence qualitatively similar to that in Fig. 2 [23]. However, the absolute scale of the torque was not determined in that experiment because the magnetic properties of the coagulations were unknown. The linear dependence of the elastic torque on angle of rotation can be understood quantitatively by mapping the problem of the disk with homeotropic anchoring onto the related problem of a rodlike inclusion with longitudinal anchoring first studied theoretically by Brochard and de Gennes [24] and investigated experimentally by Lapointe et al. [15]. The theory exploits an analogy between the elastic energy of the nematic and the electrostatic field energy of an object at fixed potential to predict that the elastic energy varies with particle orientation as

$$U = 2\pi K C \theta^2, \qquad (2)$$

where K is the Frank elastic constant within a one-elastic-constant approximation, and C is the capacitance of the particle. For a high-aspect-ratio disk, $C \approx \frac{2R}{\pi}$ [28]. This expression for the energy implies the proportionality constant between torque and angle is $A = 4\pi K C$. For comparison, using $K = 5$ pN [29], the theory predicts $A = 200$ pN μm/radian for a 5 μm disk, in good agreement with our experimental findings.

B. Topological transition at large θ

The symmetry of the director field dictates that the torque on a disk should be symmetric about $\theta = \pi/2$. However, in previous experiments with colloidal rods with longitudinal anchoring, where the same symmetry argument applies, the torque was observed to continue to increase linearly with θ to angles exceeding $\pi/2$, so that the director assumed a highly distorted, metastable configuration for $\theta > \pi/2$ [14]. In contrast, we have observed director configurations around a disk at $\theta > \pi/2$ to be unstable, leading to a topological transition in which $\theta \rightarrow \pi - \theta$. This transition is observed when the applied magnetic field is changed so that the disk passes through $\theta = \pi/2$. We have tracked this process in measurements in which the field is changed suddenly, causing the disk to rotate to angles above $\pi/2$. Figure 3(a) shows a series of images of a disk in a homeotropic cell during the transition. As the disk rotates through $\pi/2$, a defect loop is shed from the disk edge as seen in Fig. 3(a) at $t = 0.5$ s.
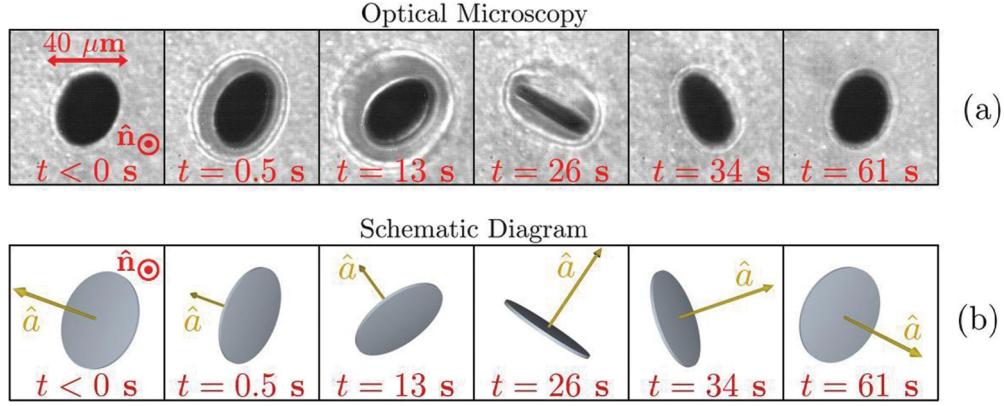
FIG. 3. (Color online) Time-lapse representations of a 20 μm disk undergoing spontaneous spinning motion that accompanies the topological transition following the disk being rotated past $\theta = \pi/2$: (a) optical microscopy images and (b) schematic diagrams illustrating the orientation of the disk. At time $t < 0$ s the disk is in a stable orientation with $\theta \approx 5\pi/22$. At $t = 0$ s the disk is rotated to an angle $\theta > \pi/2$. The images at $t = 0.5$ s show the disk immediately after its rotation past $\pi/2$. The rotation is accompanied by a pronounced distortion of the director and the shedding of a dislocation loop from the disk surface. The images at $t > 0.5$ s show the disk undergoing the spinning motion in which the component of $\hat{a}$ perpendicular to the director traverses π radians while the defect loop collapses back on the disk surface. The final state of the disk shown at $t = 61$ s is stable and resembles the initial state with $\theta \longrightarrow \pi - \theta$.

The disk then proceeds to spin such that the projection of $\hat{a}$ onto the plane perpendicular to $\hat{n}$ sweeps through π radians, as depicted schematically in Fig. 3(b). As the disk spins, the defect loop collapses back onto the disk surface. Disks appear to show no preference for the direction of this spinning; repeated experiments on the same disk show the disk spinning clockwise and counterclockwise with equal probability. As a consequence of this process, the surrounding director field is reconfigured, so that after it spins the disk no longer experiences a torque seeking to rotate it back to $\theta = 0$, but instead to $\theta = \pi$. The magnitude of the new torque is linear with the difference in θ from π. That is, the elastic energy follows a form specified by Eq. (2), with $\theta \to \pi - \theta$. The effect of this transition on the director field is depicted schematically in Fig. 4.

To understand better the complicated spinning motion of the disk during this topological transition, we have measured the time dependence of the angle β, specified in the inset to Fig. 5(a), through which the projection of $\hat{a}$ onto the plane perpendicular to $\hat{n}$ changes as the disk spins. Results for β are shown in Figs. 5(a) and 5(b) for sets of measurements on a 5 and 20 μm disk, respectively. Each measurement is initiated by a sudden change in magnetic field direction that rapidly rotates the disk through $\theta = \pi/2$. We specify the orientation before rotation by θ_i, as shown in Fig. 4(a), and the final equilibrium orientation by θ_f, where θ_f is measured with respect to the new $\theta = 0$ following the topological transition, as shown in Fig. 4(c). The change in magnetic field in the measurement is set so that the equilibrium orientations of the disk before and after spinning are symmetric about $\pi/2$, so that $\theta_f = \theta_i$. That is, the change in $\vec{B}$ is made such that the initial and final configurations are mirror images of each other. We further specify the initial and final orientations by the angle $\phi = \frac{\pi}{2} - \theta$ shown in Figs. 4(a) and 4(c). As described below, ϕ provides a convenient measure of the extent to which the disk is rotated into the unstable region by the change in magnetic field. Immediately following the change in magnetic field, before the disk begins spinning, it rotates into the unstable region to

$\theta_u > \pi/2$, as depicted in Fig. 4(b). The degree to which the disk ventures into the unstable region ($\theta > \pi/2$) can further be specified by $\phi_u = \theta_u - \frac{\pi}{2}$, as shown in Fig. 4(b). Following the rotation, the disk proceeds to spin such that β changes by π until it reaches the final orientation shown in Fig. 4(c).

Figure 5 shows sets of results for β as a function of time for different values of ϕ_u. As the results indicate, the rate of spinning depends on the degree to which the disk has been rotated into the unstable region; i.e., the spinning is faster for larger ϕ_u. In addition, β assumes a sigmoidal shape as a function of time. To model this behavior, we hypothesize that the torque on the disk that drives the transition varies with β as

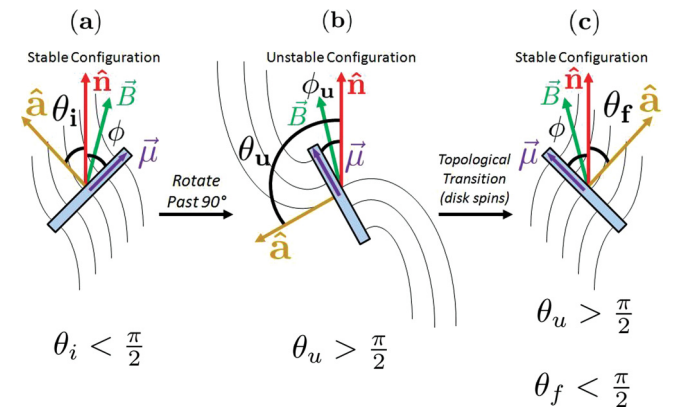$$|\vec{\tau}_s| = A_s \sin \beta. \tag{3}$$

FIG. 4. (Color online) Schematic of a disk with homeotropic surface anchoring and surrounding director configuration. (a) When a disk is rotated to an angle $\theta_i < \pi/2$, the director field surrounding the disk adopts a stable configuration that maintains long range order and local surface anchoring conditions on the disk's surface. (b) If the disk is rotated to a larger angle, $\theta_u > \pi/2$, the director configuration becomes highly distorted. (c) The spinning of the disk placed at $\theta_u > \pi/2$ accompanies a topological transition that results in a new stable configuration with $\theta_f < \pi/2$.
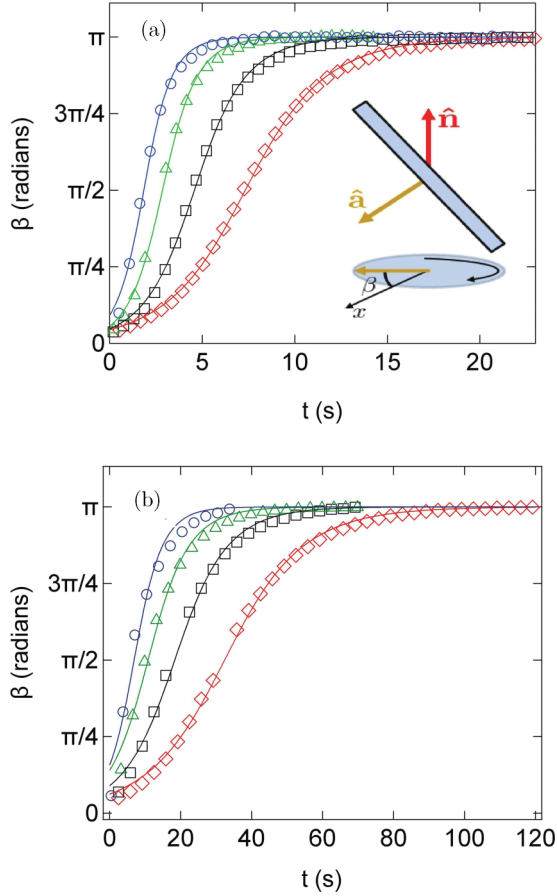
FIG. 5. (Color online) Angle through which the projection of $\hat{a}$ onto the plane perpendicular to $\hat{n}$ spins as a function of time following rotation of the disk past $\theta = \pi/2$ for (a) a 5 μm disk after being rotated to $\theta = 0.55\pi$ (red diamond), 0.59π (black square), 0.61π (green triangle), and 0.706π (blue circle) and for (b) a 20 μm disk after being rotated to $\theta = 0.59\pi$ (red diamond), 0.606π (black square), 0.656π (green triangle), and 0.767π (blue circle). Solid lines show the results of fits to the form $\beta = 2\tan^{-1}(e^{\Gamma(t-t_0)})$ as described in the text. The inset to (a) shows a schematic of the disk and its projection onto the plane perpendicular to $\hat{n}$ with β specified.

Since the spinning motion is at low Reynolds number, we assume that this torque is balanced by a drag torque, $|\vec{\tau}_D| = D_s \eta \dot{\beta}$, where D_s is the effective geometric drag coefficient and η is a drag viscosity. This balance of torques leads to the predicted time dependence

$$\beta = 2\tan^{-1}(e^{\Gamma(t-t_0)}), \qquad (4)$$

where t_0 is the time at which β passes through $\pi/2$ and $\Gamma = \frac{A_s}{D_s \eta}$ [30]. The solid lines in Fig. 3 show the results of fits to Eq. (4), which describes the time dependence well, indicating that Eq. (3) approximates accurately the form of the torque that causes the spinning. Figures 6(a) and 6(b) display results for the spinning rate Γ extracted from such fits. For both disk sizes, the rate grows approximately linearly with ϕ_u. The rate is also significantly slower for 20 μm disks compared with 5 μm disks.

Assuming that Eq. (2) continues to describe the elastic energy even as the disk is rotated into the unstable region, we can identify a simple approximation that accounts for the trends in Fig. 6. Within this assumption, the elastic energy of
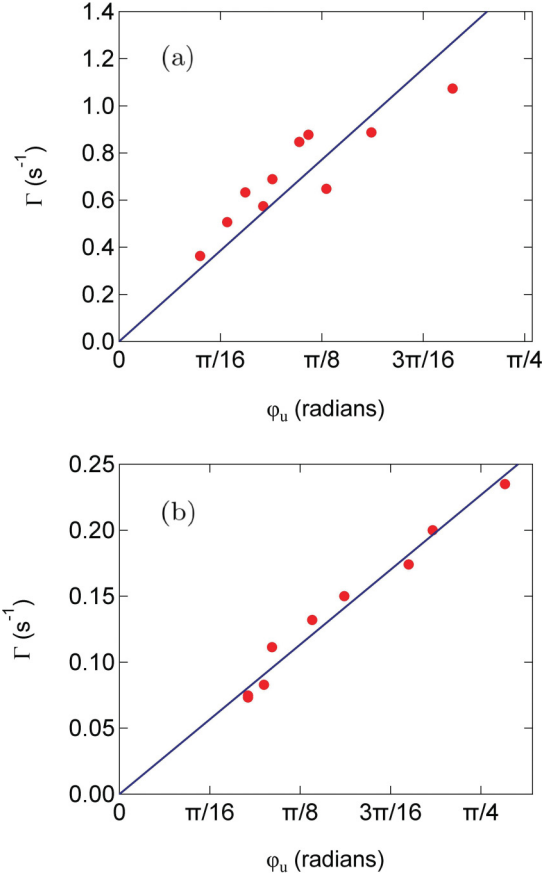

FIG. 6. (Color online) (a) The spinning rate Γ as a function of $\phi_u = \theta - \pi/2$ for (a) a 5 μm disk and (b) a 20 μm disk. The solid lines are the results of linear fits.

the unstable configuration immediately after rotation through $\pi/2$ is

$$U_u = 2\pi KC\theta_u^2 = 2\pi KC\left(\frac{\pi}{2} + \phi_u\right)^2. \qquad (5)$$

Meanwhile, the elastic energy after the topological transition is

$$U_f = 2\pi KC\theta_f^2 = 2\pi KC\left(\frac{\pi}{2} - \phi\right)^2. \qquad (6)$$

Since the magnetic field remains unchanged between when the disk is in the unstable state [Fig. 4(b)] and in the final stable state [Fig. 4(c)], balance between the magnetic and elastic torques in the two configurations dictates that θ_u is slightly less than $\pi - \theta_f$, as depicted in Figs. 4(b) and 4(c). Thus, $\phi_u < \phi$, the exact difference between the two depending on the magnitude of the applied field. However, if we neglect this difference and make the approximation $\phi_u = \phi$, then comparison of Eqs. (5) and (6) gives the change in stored elastic energy due to the topological transition as

$$\Delta U = U_f - U_u \approx -4\pi^2 KC\phi. \qquad (7)$$

When the disk spins, this energy is presumably lost to viscous dissipation, which we can approximate as

$$E_d \approx \int_0^\pi |\vec{\tau}_D|\, d\beta. \qquad (8)$$

Converting this expression to an integral over time and using Eq. (4) gives

$$E_d = \int_{-\infty}^{\infty} D_s \eta \dot{\beta}^2 \, dt = \int_{-\infty}^{\infty} \frac{4 D_s \eta \Gamma^2 e^{2\Gamma(t-t_0)}}{(1 + e^{2\Gamma(t-t_0)})^2} \, dt. \quad (9)$$

Using the relation $\int_{-\infty}^{\infty} \frac{e^u}{(1+e^u)^2} \, du = 1$ and $D_s = \frac{32}{3} R^3$, which is the geometric coefficient for rotation of the symmetry axis of a highly oblate ellipsoid [31,32], leads to

$$E_d = \frac{64}{3} \eta R^3 \Gamma. \quad (10)$$

Equating this dissipation with the change in stored energy, $E_d = -\Delta U$, hence predicts that Γ and ϕ are proportional, consistent with the results in Fig. 6, and further that the proportionality constant is

$$\frac{\Gamma}{\phi} = \frac{3\pi K}{8\eta R^2}. \quad (11)$$

Using $K = 5$ pN and $\eta = 69$ mPa s (the average of the three Miescowicz coefficients of 5CB at room temperature [33]) leads to $\frac{\Gamma}{\phi} = 3.4$ s^{-1} for $R = 5$ μm and $\frac{\Gamma}{\phi} = 0.21$ s^{-1} for $R = 20$ μm. The experimental values determined from the fits shown in Fig. 6 are 2.0 and 0.29 s^{-1} for $R = 5$ and $R = 20$ μm, respectively, in reasonable agreement with these calculated values considering the approximations entering the calculation. The outstanding question that this analysis raises, however, is why the spinning torque that drives the topological transition follows the sinusoidal form given in Eq. (3).

C. Angular relaxation

When a disk held at $\theta > 0$ is released, the elastic torque will rotate it back to $\theta = 0$. Figure 7 shows the results of measurements of θ as a function of time during this motion for a 5 and a 20 μm disk. As the results indicate, θ follows a quasi-exponential decay during this relaxation. Since the motion is at low Reynolds number (Re $\sim 10^{-6}$), inertial effects can be neglected, and hence balance between the elastic torque and viscous drag torque is maintained during relaxation. A second dimensionless parameter that is important in dictating the motion is the Ericksen number Er, which is the ratio of the viscous forces to elastic forces acting on the nematic. For a colloid of size R moving through a nematic, Er $= \frac{\eta R v}{K}$ [34], where v is the velocity of the colloid. Theory and simulations studies of colloidal motion in nematics, which have primarily focused on the translational motion of spheres, have found that the director becomes significantly affected by the flow above an Ericksen number in the range Er $\sim 1 - 10$, depending on details of the calculations [34–36]. Using $v = R\dot{\theta}$ for the disks undergoing angular relaxation, we find Er ≈ 1 for $R = 5$ μm and Er ≈ 2 for $R = 20$ μm when θ is near $\pi/2$ where the angular velocities are largest, and Er progressively decreases as θ relaxes toward zero. Thus, the Ericksen numbers characterizing the disk's motion during the angular relaxation are modest, but not so small that one can dismiss possible effects of the motion on the director. To test whether such effects are present, we assume the motion is in the limit of small Er, and determine whether the measurements are consistent with this assumption. At low Er, the elastic torque on the disk as it rotates should match the torque on the disk when it is static. In this case, the torque balance at low Re implies that θ
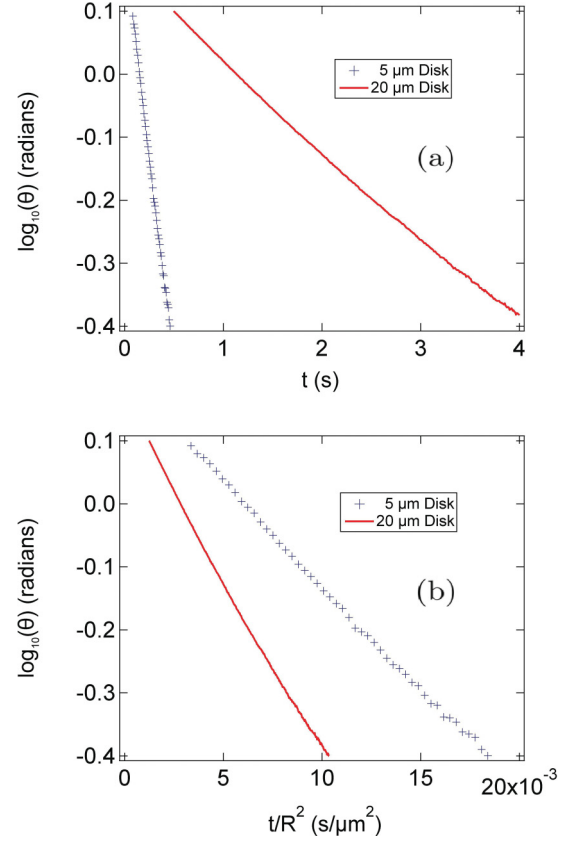

FIG. 7. (Color online) (a) Angle between the disk normal and the unperturbed director for 5 μm (blue cross) and 20 μm (red line) disks as a function of time as the disks relax to the minimum energy orientation $\theta = 0$. (b) Results for the angle plotted with time scaled by the square of the disk radius. $t = 0$ is taken when $\theta = \pi/2$.

follows the equation of motion

$$4\pi K C\theta + D\eta(\theta)\dot{\theta} = 0, \quad (12)$$

where again $D = \frac{32}{3} R^3$ is the geometric drag coefficient for rotation of the symmetry axis of a highly oblate ellipsoid, and $\eta(\theta)$ is the drag viscosity, which in general can depend on the disk orientation due to the anisotropy of the nematic.

For an isotropic fluid with uniform viscosity [$\eta(\theta) =$ constant], Eq. (12) leads to an exponential decay in $\theta(t)$ with decay rate $\gamma = \frac{3K}{4\eta R^2}$. As the results in Fig. 7(a) indicate, the angular relaxation of the disks follows roughly such an exponential decay but also shows clear deviations from it. One possible interpretation for these deviations is that they result from the nematic's anisotropic viscosity [15]. However, a second interpretation is that they reflect velocity-dependent elastic torque and drag viscosity as a consequence of the motion being outside the limit of small Er. To test whether the small-Er approximation and hence Eq. (12) are indeed valid, we note that Eq. (12) implies that the rate of relaxation scales as R^{-2}. Figure 7(b) shows the results from Fig. 7(a) plotted with the time axis scaled accordingly. Contrary to this expectation, the scaled data do not collapse. Instead, θ for the 20 μm disk, whose motion corresponds to larger Er, relaxes at a faster rate compared with the 5 μm disk than expected based on this small-Er approximation, suggesting that the director is sufficiently affected by the flow created by the disk rotation
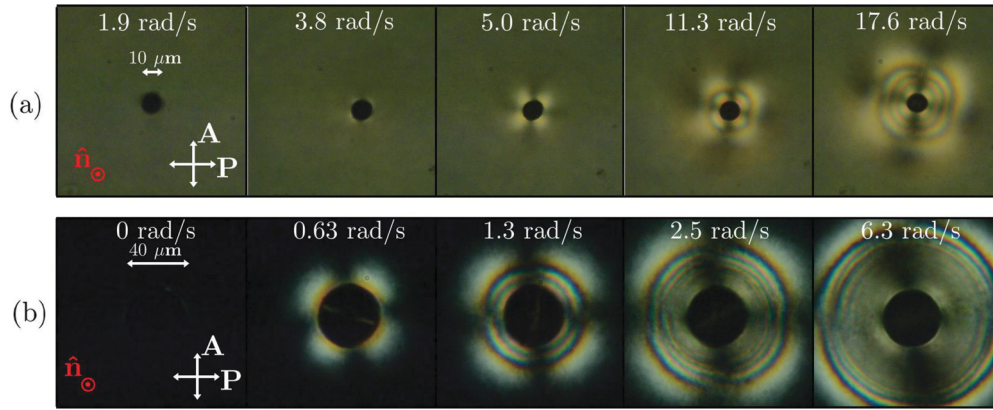
FIG. 8. (Color online) Polarization images of a (a) 5 μm and (b) 20 μm disk with homeotropic anchoring turning about the symmetry axis of the disk at various rates. Above a critical frequency a characteristic, four-lobed birefringent pattern appears indicating formation of a flow-induced vortex alignment of the director.

to alter the elastic torque and viscous drag. This conclusion is further supported by the values of effective drag viscosity extracted from the results in Fig. 7. Using best fits to an exponential decay over the span $\theta < \pi/4$, we obtain values for γ that correspond to drag viscosities of 50 and 24 mPa s for the 5 and 20 μm disks, respectively. The value for the 20 μm disk is noticeably smaller than 69 mPa s, the average of the Miescowicz coefficients of 5CB at room temperature. Such "shear thinning" is an expected consequence of flow that reorders the director.

We note another possible reason for the breakdown in the scaling in Fig. 7(b) is the proximity of the substrates and its effect on the hydrodynamic drag of the rotating disks. As mentioned above, the measurements were performed on disks that were levitated away from the bottom substrate, so that they rotated freely about an axis through their center. Nevertheless, we cannot rule out the possibility of the nearby substrates' influencing the disks' rotational mobilities. However, we expect that any effects from the proximity of the substrates would increase the hydrodynamic drag and hence slow the rotation rate and that such effects would be more prominent on the 20 μm disks than on the 5 μm disks. Specifically, the levitation left the larger disks closer to the substrate, relative to their size, than the smaller disks and the larger disks sedimented faster than the smaller disks. Contrary to this expectation, the measured rotational mobility of the 20 μm disks relative to the 5 μm disks is greater than expected. Combined with the evidence for flow-induced director reorientation described in the next section, we believe this enhancement is evidence that the rotational motion falls outside the regime of small Er.

D. Vortex deformations formed by turning disks

Direct evidence that the rotation of the disks undergoing angular relaxation alters the director field from the static, low-Er configurations is difficult to obtain. However, images of such alterations are clearly apparent in measurements in which the disk remains at $\theta = 0$ but turns at a constant angular velocity about the symmetry axis. In the static case, this disk orientation leads to no distortion of the director, as illustrated schematically in Fig 1(a). However, above a certain turning rate, the director in proximity to the disk undergoes

flow-induced alignment into a vortex-shaped pattern. To image the director around disks turning in this way, we have performed polarization microscopy measurements employing a four-axis magnetic tweezer stage described previously [37]. The stage can generate spatially uniform fields with time-independent magnitude that rotate at a constant rate either in the microscope focal plane or in a plane perpendicular to the focal plane. Figure 8(a) displays a series of polarization images showing the birefringent texture around a 5 μm disk turning at various frequencies ω in a cell with homeotropic anchoring. Figure 8(b) displays a similar series for a 20 μm disk. At low frequency (e.g., $\omega = 1.9$ rad s^{-1} for the 5 μm disk), the region around the disk remains uniformly dark when viewed through crossed polarizers, indicating that the uniformly aligned director is unaffected by the flow induced by the turning disk. Above some critical frequency, however, a characteristic four-lobed birefringent texture develops around the disk. The size and intensity of this pattern grows with increasing ω. Figure 9 shows a polarization image of a 20 μm disk turning in the same way in a planar cell, where the
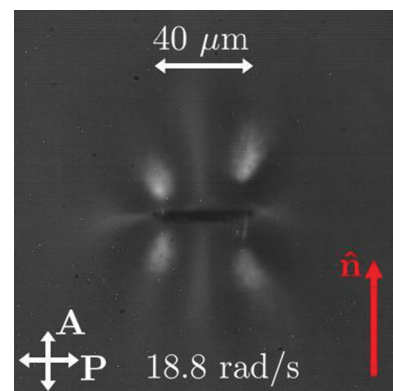

FIG. 9. (Color online) Polarization image of a 20 μm disk with homeotropic anchoring turning about the symmetry axis in a planar liquid-crystal cell in which the optical axis of the microscope is parallel to the disk's face. Produced is a pattern with eight bright regions surrounding the disk illustrative of the director-field deformations generated by the fluid flow.
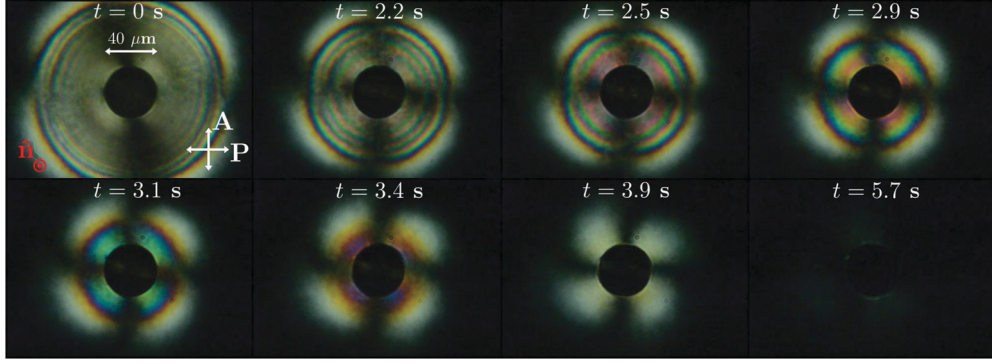
FIG. 10. (Color online) Time-lapse series of polarization images of a 20 μm disk with homeotropic anchoring showing the shrinking and decay of the flow-induced birefringent texture after the disk stops turning about its symmetry axis. The disk, initially turning at $\omega = 6.3$ rad s^{-1}, is stopped at $t = 0$ and is stationary at later times.

distortion pattern above and below the disk is observable. Identifying precisely the critical frequency that marks the onset of the flow-induced director distortions is difficult and somewhat subjective because at frequencies near the onset the spatial extent of the affected region is small [see, e.g., $\omega = 3.8$ rad s^{-1} for the 5 μm disk in Fig. 8(a)], and its visibility depends on factors such as the microscope condenser brightness. Nevertheless, we estimate the critical frequencies to be roughly $\omega_c \approx 3$ and 0.3 rad s^{-1} for 5 and 20 μm disks, respectively. From the relation for the Ericksen number, Er $= \frac{\eta \omega R^2}{K}$, these critical frequencies correspond to critical Ericksen numbers of 1.0 and 1.6 for 5 and 20 μm, respectively. Thus, these observations illustrate that, albeit for a different motion of the disk than in the angular relaxation described in Sec. III C, the director becomes affected by the motion at Ericksen numbers comparable to those realized in the angular relaxation measurements.

We stress that the nematic distortions created by the turning disks illustrated in Figs. 8 and 9 have a purely hydrodynamic origin. When the magnetic field is removed, the disks stop turning essentially immediately (consistent with low-Re hydrodynamics) and display no measurable recoil that would indicate any elastic energy stored in the nematic. After a disk stops turning, the surrounding deformation pattern steadily shrinks in size and fades away. This process is illustrated in Fig. 10, which displays a series of polarization images of the director field around a 20 μm disk at various times after the disk has stopped turning. A very similar process follows the cessation of turning of the 5 μm disks, except more quickly. We identify the time scale for the decay of the distortion with the elastic relaxation time $\eta R^2 / K$ [1], which is approximately 0.35 and 5.5 s for 5 and 20 μm disks, respectively. We note that these values for the elastic relaxation time are comparable with the time during which the disks rotate back to $\theta = 0$ in the angular relaxation, as shown in Fig. 7(a), further suggesting a breakdown in the static, low-Er approximation underlying Eq. (12) as an explanation for the failure of the scaling in Fig. 7(b). These observations of disks turning about their axis and the nematohydrodynamic response that is induced hence provide a helpful illustration of the limits to low-Er colloidal motion in nematics.

IV. CONCLUSION

In conclusion, these experiments to investigate the static and dynamic behavior of disk-shaped colloids in a nematic illustrate several important points regarding the properties of aspherical particles dispersed in liquid crystals. The electrostatic analogy, which quantitatively accounts for the elastic torque on a disk as described in Sec. III A, provides a straightforward framework to determine the distorted director field in the surrounding fluid. A key feature of this distortion is its predictable dependence on disk orientation, which suggests a potential new avenue for engineering colloidal interactions in liquid crystals. To date, a number of approaches have been explored for varying liquid-crystal-mediated interactions, and hence the type of ordered structures colloids form when they self-assemble, by altering the director distortion around particles. For instance, extensive previous research on spherical colloids has demonstrated how changes in anchoring conditions at the particle surfaces lead to different self-assembled structures [6]. Additional recent studies have shown [7] how aspherical colloids can be subject to shape-specific interactions in liquid crystals by virtue of the shape dependence to the distortion, and exploiting this dependence has been proposed as another approach for engineering colloidal interactions and self-assembled structures [18]. The orientation-dependent distortions around aspherical particles illustrated in our experiments on disks thus introduce a third possible mechanism for controlling colloidal interactions, and an interesting next step for research in this area would be to investigate pair interactions engendered by these distortions. Indeed, the ability to tune the distortions by adjusting particle orientation, such as with a magnetic field for magnetic colloids, suggests that this mechanism for engineering interactions could be particularly versatile. However, as the topological transition in the director field described in Sec. III B illustrates, the range of stable deformations that can be achieved by controlling orientation has limits. Another important consideration in employing liquid-crystal-mediated interactions for colloidal self-assembly is the dynamics of the process. As such interactions are exploited to construct increasingly intricate colloidal assemblies [38–40], which in many cases are metastable, the details of the colloids' motion during the

assembly become increasingly important. The effect of this motion on the director field, which the results in Sec. III D indicate can occur at modest Ericksen number, hence has potential implications for the interactions. Further study of such colloidal dynamics should be a focus of future work on particle dispersions in liquid crystals.

[1] P. G. de Gennes and J. Prost, *The Physics of Liquid Crystals*, 2nd ed. (Oxford University Press, Oxford, 1995).

[2] D. C. Wright and N. D. Mermin, Rev. Mod. Phys. **61**, 385 (1989).

[3] H. Stark, Phys. Rep. **351**, 387 (2001).

[4] Y. Gu and N. L. Abbott, Phys. Rev. Lett. **85**, 4719 (2000).

[5] P. Poulin, H. Stark, T. C. Lubensky, and D. A. Weitz, Science **275**, 1770 (1997).

[6] I. Mušević and M. Škarabot, Soft Matter **4**, 195 (2008).

[7] C. P. Lapointe, T. G. Mason, and I. I. Smalyukh, Science **326**, 1083 (2009).

[8] U. Tkalec, M. Škarabot, and I. Mušević, Soft Matter **4**, 2402 (2008).

[9] J. B. Rovner, C. P. Lapointe, D. H. Reich, and R. L. Leheny, Phys. Rev. Lett. **105**, 228301 (2010).

[10] C. J. Smith and C. Denniston, J. Appl. Phys. **101**, 014305 (2007).

[11] D. Andrienko, M. P. Allen, G. Skačej, and S. Žumer, Phys. Rev. E **65**, 041702 (2002).

[12] C. P. Lapointe, D. H. Reich, and R. L. Leheny, Langmuir **24**, 11175 (2008).

[13] B. I. Lev, S. B. Chernyshuk, P. M. Tomchuk, and H. Yokoyama, Phys. Rev. E **65**, 021709 (2002).

[14] C. Lapointe, A. Hultgren, D. M. Silevitch, E. J. Felton, D. H. Reich, and R. L. Leheny, Science **303**, 652 (2004).

[15] C. Lapointe, N. Cappallo, D. H. Reich, and R. L. Leheny, J. Appl. Phys. **97**, 10Q304 (2005).

[16] C. P. Lapointe, S. Hopkins, T. G. Mason, and I. I. Smalyukh, Phys. Rev. Lett. **105**, 178301 (2010).

[17] P. M. Phillips, N. Mei, L. Reven, and A. Rey, Soft Matter **7**, 8592 (2011).

[18] J. Dontabhaktuni, M. Ravnik, and S. Žumer, Soft Matter **8**, 1657 (2012).

[19] F. R. Hung, O. Guzmán, B. T. Gettelfinger, N. L. Abbott, and J. J. de Pablo, Phys. Rev. E **74**, 011711 (2006).

[20] D. Andrienko, M. Tasinkevych, P. Patrício, M. P. Allen, and M. M. Telo da Gama, Phys. Rev. E **68**, 051702 (2003).

[21] F. R. Hung, Phys. Rev. E **79**, 021705 (2009).

[22] S. Hernàndez-Navarro, P. Tierno, J. Ignés-Mullol, and F. Sagués, Soft Matter **7**, 5109 (2011).

[23] C. F. Hayes, Mol. Cryst. Liq. Cryst. **36**, 245 (1976).

[24] F. Brochard and P. G. de Gennes, J. Phys. (Paris) **31**, 691 (1970).

[25] H. Lamb, *Hydrodynamics*, 6th ed. (Dover Publications, New York, 1945).

[26] C. M. Noel, F. Giulieri, R. Combarieu, G. Bossis, and A. M. Chaze, Colloids Surf. A **295**, 246 (2007).

[27] O. P. Pishnyak, S. Tang, J. R. Kelly, S. V. Shiyanovskii, and O. D. Lavrentovich, Phys. Rev. Lett. **99**, 127802 (2007).

[28] L. D. Landau and E. M. Lifshitz, *Electrodynamics of Continuous Media* (Pergamon Press, New York, 1960).

[29] N. V. Madhusudana and R. Pratibha, Mol. Cryst. Liq. Cryst. **89**, 249 (1982).

[30] A. Anguelouch, R. L. Leheny, and D. H. Reich, Appl. Phys. Lett. **89**, 111914 (2006).

[31] B. J. Berne and R. Pecora, *Dynamic Light Scattering: With Applications to Chemistry, Biology, and Physics* (Dover Publications, New York, 2000).

[32] As illustrated in Fig. 3(b), the spinning motion is somewhat more complicated than a simple rotation of the symmetry axis $\hat{a}$, so use of this form for the geometric coefficient should be considered an approximation.

[33] A. G. Chmielewski, Mol. Cryst. Liq. Cryst. **132**, 339 (1986).

[34] B. T. Gettelfinger, J. A. Moreno-Razo, G. M. Koenig Jr., J. P. Hernández-Ortiz, N. L. Abbott, and J. J. de Pablo, Soft Matter **6**, 896 (2010).

[35] H. Stark and D. Ventzki, Europhys. Lett. **57**, 60 (2002).

[36] C. Zhou, P. Yue, and J. J. Feng, J. Fluid Mech. **593**, 385 (2007).

[37] M. H. Lee, C. P. Lapointe, D. H. Reich, K. J. Stebe, and R. L. Leheny, Langmuir **25**, 7976 (2009).

[38] I. Mušević, M. Škarabot, U. Tkalec, M. Ravnik, and S. Žumer, Science **313**, 954 (2006).

[39] U. Ognysta, A. Nych, V. Nazarenko, I. Mušević, M. Škarabot, M. Ravnik, S. Žumer, I. Poberaj, and D. Babič, Phys. Rev. Lett. **100**, 217803 (2008).

[40] M. Škarabot, M. Ravnik, S. Žumer, U. Tkalec, I. Poberaj, D. Babič, and I. Mušević, Phys. Rev. E **77**, 061706 (2008).